Transfer Coefficients from Air-gap to Stator Bore Radius for Magnetic Force Wavenumbers - Application to Electrical Machines

Raphaël Pile[1,2,3], Jean Le Besnerais[2], Guillaume Parent[3], Yvonnick Le Menach[1], Emile Devillers[2], Thomas Henneron[1], and Jean-Philippe Lecointe[3]

[1]Univ. Lille, Arts et Metiers ParisTech, Centrale Lille, HEI, EA 2697 - L2EP -Laboratoire d'Electrotechnique et d'Electronique de Puissance, F-59000 Lille, France
[2]EOMYS ENGINEERING, Lille-Hellemmes 59260, France
[3]Univ. Artois, EA 4025, Laboratoire Systèmes Électrotechniques et Environnement (LSEE), F-62400 Béthune, France

June 28, 2019

Abstract

The Maxwell Stress Tensor (MST) method is commonly used to accurately compute the global efforts, such as electromagnetic torque ripple and unbalanced electromagnetic forces in electrical machines. The MST has been extended to the estimation of local magnetic surface force for the vibroacoustic design of electrical machines under electromagnetic excitation. In particular one common air-gap surface force method based on MST is to compute magnetic surface forces on a cylindrical shell in the air-gap. This air-gap surface force method is well-adapted to compute local magnetic surface forces from analytical air-gap field methods - such as methods based on permeance and magneto-motive force (PMMF) - because these air-gap field methods can only predict the magnetic field in the middle of the air-gap. However the air-gap surface force distribution depends on the radius of the cylindrical shell. This paper main contribution is to demonstrate an analytic transfer law of the air-gap surface force between the air-gap and the stator bore radius. It allows to quantify the error between the magnetic surface force calculated in the middle of the air-gap and the magnetic force computed on the stator teeth. This paper shows the strong influence of the transfer law on the computed tangential surface force distribution through numerical applications with induction and synchronous electrical machines. However the demonstrated transfer law keeps the global electromagnetic torque constant for any radius. At last the surface force density at stator bore radius is more accurately estimated when applying the new transfer law on the air-gap surface force.

1 Introduction

The Maxwell Stress Tensor (MST) method based on a closed surface is commonly used to accurately compute the electromagnetic torque and global forces in electrical machines [1–5]. The issue of local magnetic forces computation has been addressed in many publications from the electromagnetic energy derivation [1,6–8] to the application of numerical methods [9–11]. However, recent developments in the field of electromagnetic vibrations for electrical machines show a preference for estimating local magnetic forces based on the MST in the air-gap [12–18].

The Air-Gap Surface Force (AGSF) method based on MST consists in computing equivalent magnetic surface forces with a cylindrical shell in the middle of the air-gap. The AGSF is based on the assumption that the air-gap is relatively thin in electrical machines, and that the difference will be negligible for vibro-acoustic analysis. This paper proposes to discuss these assumptions. The popularity of the methods based on AGSF is mainly due to the compatibility of the method with analytical modelling techniques as permeance and magneto-motive force (MMF) [19–23]. Indeed, analytical models are able to calculate the magnetic field of the electric machine only in the middle of the air-gap. Thus only the AGSF is available to estimate magnetic excitation. Alternatively, semi-analytical methods [24,25] are able to calculate the magnetic field in the whole air-gap band. A downside of this approach is Gibbs phenomenon [26] that reduces the accuracy of AGSF computed on the stator bore radius. The energy derivation methods are not compatible with analytical and semi-analytical methods to compute magnetic local forces as the knowledge of the magnetic field is not available everywhere in the electrical machine. As a consequence only the AGSF method is available for analytical methods.

Nevertheless, the compatibility with analytical and semi-analytical methods allows to perform fast vibroacoustic design, optimization and troubleshoot at low computational cost [21,22]. Indeed, the AGSF is also compatible with Frequency Response Function (FRF) based on mechanical analytical models for vibration prediction [27,28]: thanks to an angular Fourier transform of the AGSF, the vibration response to each AGSF wavenumber can be performed. Then, the most harmful excitation can be identified. This magneto-mechanical coupling is also used with mechanical Finite Element Analysis (FEA) because the angular wavenumber decomposition along a circular path allows to troubleshoot the electromagnetic sources of vibrations [29].

The AGSF is used to calculate equivalent distributed forces at the neutral fiber of the stator yoke [22] or on the tip of the stator teeth [30]. Several models have recently been proposed to compute from the AGSF the equivalent forces which applies to the neutral fiber [31,32]. In some cases, the AGSF are integrated as lumped tooth forces [14,33].

The variation of AGSF as a function of radius was mainly studied numerically [34]: the AGSF position has an effect on vibration results at high frequency. This is consistent with the study [35] which shows an analytical dependency of AGSF results with radius and angular wavenumber for a theoretical slotless machine. The analytical calculation of global forces and torque - which correspond to the integral of the 0^{th} AGSF wavenumbers - have been studied in [36,37]. The analytic study of higher AGSF wavenumbers is one objective of the paper.

The main contribution of the paper is to demonstrate the new analytic transfer law (43) which allows to compute the AGSF at the stator teeth tip radius - or stator bore radius - based on the AGSF in the middle of the airgap. The new transfer law is a generalization of the solution proposed in [35]. This new transfer law allows to understand how the magnetic force wavenumbers depends on the air-gap radius of computation. It does not depend on the topology of the rotating electrical machine. The formula remains valid in the whole air-gap band, even in front of the slots. The transfer of magnetic force inside the slot is not discussed in the paper as it is not yet compatible with the fast vibroacoustic design in electrical machine.

The paper recalls the classical application of MST for AGSF. Then the transfer law is analytically demonstrated. Then examples of application highlight the improvement for the vibroacoustic design of Squirrel-Cage Induction Machine (SCIM) and Surface Permanent Magnet Synchronous Machine (SPMSM).

2 Magnetic stress Tensor

In this section the magnetic stress tensor is defined. In particular the Vacuum Maxwell stress tensor is presented.

2.1 Maxwell Stress Tensor

A given domain Ω is deformed by an infinitesimal displacement vector $\mathbf{dx}$ as illustrated in Fig. 1. The corresponding stress tensor $\mathbf{T}$ of the magnetic domain can be related to the mechanical work done per unit area δW such that :

$$\delta W = -\mathbf{n} \cdot \mathbf{T} \cdot \mathbf{dx} \tag{1}$$

with $\mathbf{n}$ the normal vector to the unit area. An illustration is provided in Fig. 1 where the red unit surface produces a mechanical work given by (1).

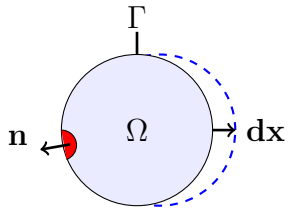

Figure 1: Illustration of the energy theorem on a magnetic domain

According to [6,7], for an incompressible linearly magnetizable media - $\forall \mathbf{x} \in \Omega$, $\mathbf{B}(\mathbf{x}) = \mu(\mathbf{x}, B)\mathbf{H}(\mathbf{x})$ - the magnetic stress tensor reduces to $\mathbf{T}_\mathrm{m}$ which is referred to as MST:

$$\mathbf{T}_\mathrm{m} = -\mu \frac{|\mathbf{H}|^2}{2}\mathbf{I} + \mu \mathbf{H}\mathbf{H} \tag{2}$$

In particular, the Vacuum MST is obtained for $\mu = \mu_0$.

2.2 Air-gap Maxwell Tensor

The total magnetic force $\mathbf{F}_\mathrm{m}$ applied on a domain V can be obtained by integrating the divergence of $\mathbf{T}_\mathrm{m}$ into a volume Ω containing V:

$$\mathbf{F}_\mathrm{m} = \int_\Omega \nabla \cdot \mathbf{T}_\mathrm{m} \, \mathrm{d}\Omega \tag{3}$$

Supposing Ω is a compact subset of $\mathbb{R}^3$ with a piece-wise smooth closed boundary Γ, and since $\mathbf{T}_\mathrm{m}$ is continuously differentiable on Ω and defined on a neighborhood of Ω, then the Gauss's theorem [38] can be applied:

$$\mathbf{F}_\mathrm{m} = \oint_\Gamma \mathbf{T}_\mathrm{m} \cdot \mathbf{n} \, \mathrm{d}\Gamma \tag{4}$$

where $\mathbf{n}$ is the outward pointing unit normal field of the closed boundary Γ. If V is surrounded by non-magnetic material (by example air or void) then Γ can be extended to this non-magnetic domain without changing the total magnetic force or torque acting on V.

In the case of electrical machine the computed total force is the same for any continuous surface in the air gap, even one that wiggles and changes radius. If B_n and H_t are the magnetic fluxes locally normal (resp. magnetic field locally tangential) to Γ, then integrating the MST (2) along Γ in the air-gap - as in Fig.2 - leads to:

$$\mathbf{F}_\mathrm{m} = \oint_\Gamma \left(-\frac{\mu_0}{2} H^2 \mathbf{n} + \mu_0 H_\mathrm{n} \mathbf{H} \right) \, \mathrm{d}\Gamma \tag{5}$$

At this point, the term under the integral sign has the dimension of a surface force density denoted $\mathbf{P}_\mathrm{ag}$. By developing $\mathbf{P}_\mathrm{ag}$ and using the closure relationship $\mathbf{B} = \mu_0 \mathbf{H}$, this AGSF becomes:

$$\mathbf{P}_\mathrm{ag} = \left(\frac{1}{2\mu_0} B_\mathrm{n}^2 - \frac{\mu_0}{2} H_\mathrm{t}^2 \right) \mathbf{n} + B_\mathrm{n} H_\mathrm{t} \mathbf{t} \tag{6}$$

where $\mathbf{t}$ is the unit tangential field associated to $\mathbf{n}$. Expression (6) is usually applied on a cylindrical surface Γ in the middle of the air-gap [5,12–18,33]. An example is provided in Fig. 2 with the blue dashed surface Γ. With cylindrical surfaces, the normal direction $\mathbf{n}$ is opposite to the radial direction $\mathbf{e}_\mathrm{r}$ when considering the forces experienced by the external structure. Then, the surface force (6) can be decomposed as a sum of a radial and tangential contribution $\forall \theta \in [0, 2\pi]$ and for all radius r inside the air-gap cylindrical band:

$$\mathbf{P}_\mathrm{ag}(r, \theta) = P_\mathrm{r}(r, \theta) \mathbf{e}_\mathrm{r} + P_\theta(r, \theta) \mathbf{e}_\theta \tag{7}$$

such that the formula to compute AGSF becomes:

$$\begin{aligned} P_\mathrm{r}(r, \theta) &= -\left(\frac{1}{2\mu_0} B_\mathrm{r}^2(r, \theta) - \frac{\mu_0}{2} H_\theta^2(r, \theta) \right) \\ P_\theta(r, \theta) &= -B_\mathrm{r}(r, \theta) H_\theta(r, \theta) \end{aligned} \tag{8}$$

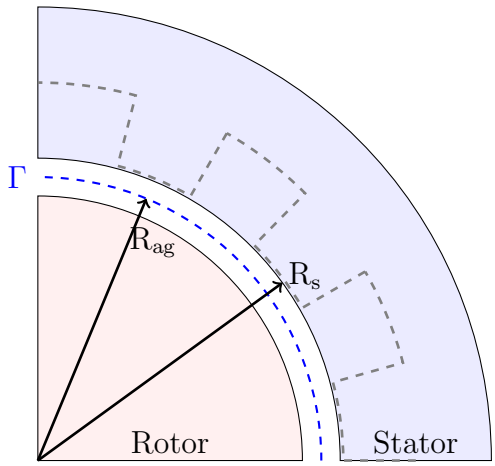

Figure 2: Illustration of the air-gap Maxwell Tensor application

The advantage of using (8) is that global magnetic forces in the cartesian referential - as well as electromagnetic torque - are theoretically independent of the selected closed surface Γ. On the other hand, the surface force density (8) varies depending on Γ [34,35].

2.2.1 Surface force density on tooth tip

The properties of $\mathbf{T}_{\mathrm{m}}$ allow to compute the surface magnetic force density $\mathbf{p}$ at the interface between a domain 1 and a domain 2 as illustrated in Fig. 3. Indeed, a magnetic stress tensor $\mathbf{T}_{\mathrm{m},1}$ associated with domain 1 generates a surface force density $\mathbf{p}_1$ on Γ:

$$\mathbf{p}_1 = \mathbf{n}_{1,2} \cdot \mathbf{T}_1 = -\mathbf{n}_{2,1} \cdot \mathbf{T}_1 \tag{9}$$

where $\mathbf{n}_{1,2}$ is the outward pointing unit normal vector. Another contribution $\mathbf{p}_2$ is obtained when considering the domain 2. The resultant surface force density $\mathbf{P}_{\mathrm{surf}}$ is obtained by applying (9) on both sides of Γ:

$$\mathbf{P}_{\mathrm{surf}} = \mathbf{p}_1 + \mathbf{p}_2 \tag{10}$$

As a consequence, magnetic surface forces come from a permeability gap. In electrical machines, the magnetic surface forces of interest are mainly located on stator teeth tip at the interface between the air and a ferromagnetic

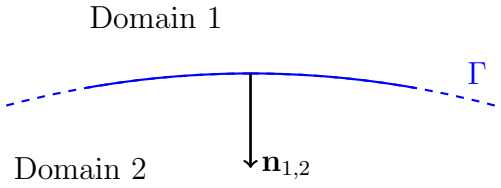

Figure 3: Surface force density calculation

media:

$$\begin{aligned} \mathbf{p}_{air} &= \left\{ \frac{1}{2\mu_0} B_{\mathrm{n}}^2 - \frac{\mu_0}{2} H_{\mathrm{t}}^2 \right\} \mathbf{n} \\ \mathbf{p}_{iron} &= -\left\{ \frac{1}{2\mu} B_{\mathrm{n}}^2 - \frac{\mu}{2} H_{\mathrm{t}}^2 \right\} \mathbf{n} \end{aligned} \tag{11}$$

Then the surface force density applying to the ferromagnetic media becomes [8,39,40]:

$$\mathbf{P}_{\mathrm{surf}} = \left\{ \frac{1}{2} \left(\frac{1}{\mu_0} - \frac{1}{\mu} \right) B_{\mathrm{n}}^2 - \frac{\mu_0 - \mu}{2} H_{\mathrm{t}}^2 \right\} \mathbf{n} \tag{12}$$

Note that this expression should lead to the same results on both side of the interface since B_{n} and H_{t} are theoretically continuous. If the assumption of high relative permeability in iron is used for the vibroacoustic design of electrical machines, such that $\mathbf{p}_{iron} \approx 0$:

$$\mathbf{P}_{\mathrm{surf}} \approx \mathbf{p}_{air} \approx \left(\frac{1}{2\mu_0} B_{\mathrm{n}}^2 - \frac{\mu_0}{2} H_{\mathrm{t}}^2 \right) \mathbf{n} \tag{13}$$

Then one gets for the angular position θ corresponding to the tip of the stator teeth:

$$\mathbf{P}_{\mathrm{surf}} = \mathbf{P}_{\mathrm{ag}}(\mathrm{R_s}, \theta) \tag{14}$$

As seen in [33], magnetic forces are mainly concentrated on the tip of the stator teeth as surface forces in the case of low saturation (or high relative permeability). To reduce differences with the interface surface forces on the tooth tip (13), the AGSF (8) should be applied at the stator bore radius $\mathrm{R_s}$. However it is not possible when using analytical modelling. This is the main motivation for determining the AGSF transfer law (43).

Additionally, a transfer law could be useful even when considering electromagnetic FEA. Indeed, it is well-kown that the electromagnetic field is ill-defined at the corner of a tooth because it comes off at an angle. Moreover,

the weak-formulation used in FEA does not allow to impose both normal magnetic flux density B_n and tangential magnetic field H_t continuous at the same time. As a consequence, numerical errors increase near a discontinuity in magnetic permeability (e. g. on the tip of the teeth). An example of this issue is presented in Fig. 4-5: it is based on the slotless case from [35] where the FEA is performed with FEMM [41]. The slotless geometry is chosen to prevent errors due to an ill-defined magnetic field in the corners. These errors affect both radial and tangential forces evaluation. Vibration generated by radial forces is often predominant, however the tangential contribution should not be underestimated in the general case [30,42,43].

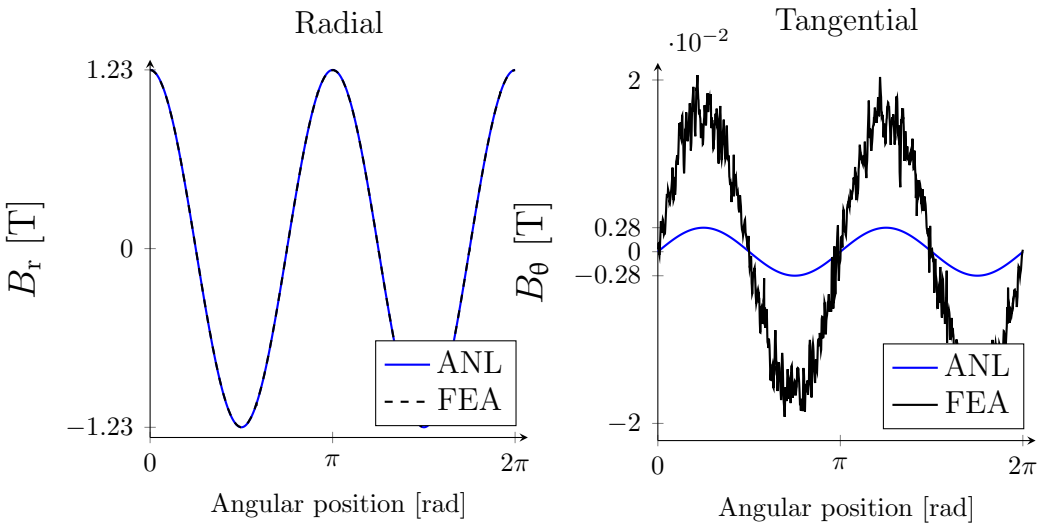

Figure 4: Comparison between analytical (ANL) and numerical (FEA) computation of the magnetic flux density components B_r and B_t at radius $r = 0.9996\mathrm{R_s}$ with a slotless machine for a wavenumber $k = 2$.

To reduce this numerical error a thinner mesh can be used at the iron/air interface but this should increase the calculation time. Then calculating AGSF with the magnetic field in the middle of the air-gap instead of the tooth tip distorted magnetic field can therefore reduce calculation cost. This is another motivation for determining the AGSF transfer law (43).

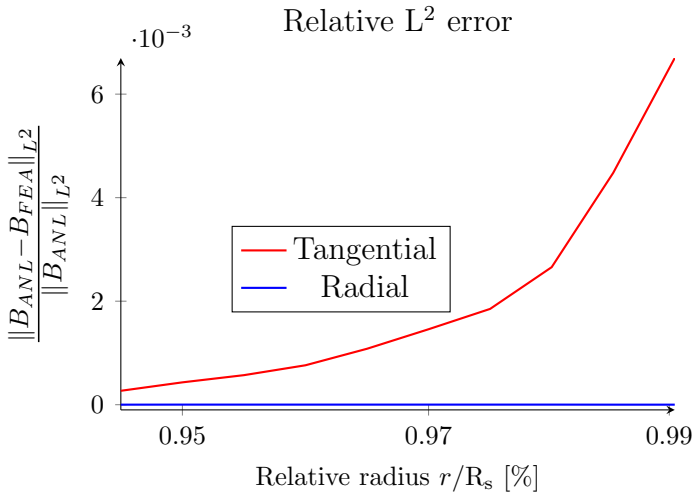

Figure 5: Comparison between analytical (ANL) and numerical (FEA) computation of the magnetic flux density components B_r and B_t depending on the radius with a slotless machine for a wavenumber $k = 2$.

2.2.2 Application to vibro-acoustic

Another reason for using the AGSF (8) based on MST is the compatibility with Electromagnetic Vibration Synthesis (EVS) [29]. The principle of EVS is to excite a structural model - analytical cylindrical shell model [27,44], 3D mechanical FEA [14,30] ... - with some unit-magnitude rotating force wave. The targeted wavenumbers are generally between 0 and 8 for the vibroacoustic analysis of electrical machines. Finally the Electromagnetic Vibration Synthesis (EVS) can be performed by multiplying each wavenumbers of the AGSF complex Fourier transform with its corresponding FRF.

The magneto-mechanical coupling based on AGSF (8) combined with FRF is of great interest for the vibroacoustic study of electrical machines because it allows a troubleshoot of the vibroacoustic behaviour from several electromagnetic sources based on the air-gap spectrum [44–46]. In particular, the tangential force response is also under investigation because it can be a significant contributor to the magnetic noise [14,30,31,42,43,47].

For all these motivations, the next sections propose to demonstrate and apply a new transfer law in order to understand the surface force behaviour in the air-gap.

3 Demonstration of transfer coefficients

The goal of this section is to analytically demonstrate the transfer law (43) and the associated transfer coefficients (44). It is supposed that the AGSF (8) is known on a circular contour in the air-gap such as the blue contour Γ in Fig. 2. To demonstrate the transfer law, the air-gap magnetic field is analytically solved with the approximation of quasi-stationary regimes and without any hypothesis on the electrical machine topology. Then the complex Fourier transform of the AGSF is computed at both air-gap radius $\mathrm{R_{ag}}$ and $\mathrm{R_s}$. Finally the different expressions are compared to get the transfer law (43). The temporal dimension is omitted because formulae remain valid at any time step. Mathematical tools and formulations are borrowed from the publications [24,48–50].

3.1 Magnetic field in the air-gap

The definition , domain required for the problem is reduced to the cylindrical air-gap band. At first, a single magnetic flux density wave of order k is considered as the boundary condition in the air-gap at the radius $r = \mathrm{R_{ag}}$:

$$\begin{aligned} B_\mathrm{r}(\mathrm{R_{ag}}, \theta) &= B_{\mathrm{r},k} \cos(k\theta + \phi_{\mathrm{r},k}) \\ B_\theta(\mathrm{R_{ag}}, \theta) &= B_{\theta,k} \cos(k\theta + \phi_{\theta,k}) \end{aligned} \tag{15}$$

It is equivalent to say that an ideal excitation is considered. It can be produced by any kind of component (electrical conductor, permanent magnets ...) but this paper does not make any distinction. Note that the radius $\mathrm{R_{ag}}$ is arbitrarily chosen in the domain of definition.

In these conditions, the fundamental equation for the electromagnetic field is the Poisson's equation [38] for the 2D magnetic vector potential component A_z in polar coordinates $\forall \theta \in [0, 2\pi]$, $\forall r \in [\mathrm{R_{ag}}, \mathrm{R_s}]$:

$$\frac{1}{r}\frac{\partial}{\partial r}\left(\frac{1}{r}\frac{\partial A_\mathrm{z}}{\partial r}\right) + \frac{\partial^2 A_\mathrm{z}}{\partial \theta^2} = 0 \tag{16}$$

A solution exists and it is unique for the previous system [51]. Then a method consists to state a function A_z and to check if it fulfills the boundary conditions. A solution similar to [24] is searched for the upper cylindrical

air-gap band $\forall\theta \in [0, 2\pi]$ and $\forall r \in [\mathrm{R_{ag}}, \mathrm{R_s}]$:

$$\begin{aligned} A(r,\theta) =& \frac{\gamma_k E_k(r, \mathrm{R_s}) + \alpha_k E_k(\mathrm{R_{ag}}, r)}{E_k(\mathrm{R_{ag}}, \mathrm{R_s})} \sin(k\theta + \phi_{\mathrm{r},k}) \\ &+ \frac{\zeta_k E_k(r, \mathrm{R_s}) + \chi_k E_k(\mathrm{R_{ag}}, r)}{E_k(\mathrm{R_{ag}}, \mathrm{R_s})} \cos(k\theta + \phi_{\theta,k}) \end{aligned} \tag{17}$$

where the unknowns γ_k, α_k, ζ_k and χ_k depends on the geometry, the wavenumber and the boundary conditions. Next step is to link the magnetic flux density with the magnetic potential:

$$\begin{aligned} B_\mathrm{r}(r,\theta) &= \frac{1}{r}\frac{\partial A}{\partial \theta}(r,\theta) \\ B_\theta(r,\theta) &= -\frac{\partial A}{\partial r}(r,\theta) \end{aligned} \tag{18}$$

Then, the boundary condition (15) allows to determine the previous unknowns:

$$\begin{aligned} \gamma_k &= \frac{\mathrm{R_{ag}}}{k} B_{\mathrm{r},k} \\ \alpha_k &= \frac{\mathrm{R_{ag}}}{k} B_{\mathrm{r},k} \frac{F_k(\mathrm{R_{ag}}, \mathrm{R_s})}{2} \\ \zeta_k &= 0 \\ \chi_k &= \frac{\mathrm{R_{ag}}}{k} B_{\theta,k} \frac{E_k(\mathrm{R_{ag}}, \mathrm{R_s})}{2} \end{aligned} \tag{19}$$

Thus the magnetic potential inside the air-gap band is entirely determined. The corresponding magnetic flux density is deduced from the knowledge of (17) and (19):

$$\begin{aligned} B_\mathrm{r}(\mathrm{R_s},\theta) =& \frac{\mathrm{R_{ag}}}{\mathrm{R_s}} \left(B_{\mathrm{r},k} \frac{F_k(\mathrm{R_{ag}}, \mathrm{R_s})}{2} \cos(k\theta + \phi_{\mathrm{r},k}) \right. \\ &\left. - B_{\theta,k} \frac{E_k(\mathrm{R_{ag}}, \mathrm{R_s})}{2} \sin(k\theta + \phi_{\theta,k}) \right) \\ B_\theta(\mathrm{R_s},\theta) =& \frac{\mathrm{R_{ag}}}{\mathrm{R_s}} \left(B_{\mathrm{r},k} \frac{E_k(\mathrm{R_{ag}}, \mathrm{R_s})}{2} \sin(k\theta + \phi_{\mathrm{r},k}) \right. \\ &\left. + B_{\theta,k} \frac{F_k(\mathrm{R_{ag}}, \mathrm{R_s})}{2} \cos(k\theta + \phi_{\theta,k}) \right) \end{aligned} \tag{20}$$

This result is generalizable to a multi-wavenumber magnetic problem thanks to the linear property of the Poisson Equation [38,51]: a linear combination of solutions of the form (20) for different value of n is still a solution of (16). Using the following complex notation:

$$\begin{aligned} \underline{B_{\mathrm{r},k}} &= B_{\mathrm{r},k}\mathrm{e}^{j\phi_{\mathrm{r},k}} \\ \underline{B_{\theta,k}} &= B_{\theta,k}\mathrm{e}^{j\phi_{\theta,k}} \end{aligned} \tag{21}$$

the air-gap magnetic flux density can be decomposed as complex Fourier series:

$$\begin{aligned} B_{\mathrm{r}}(\mathrm{R_{ag}},\theta) &= \sum_{k=-\infty}^{k=+\infty} \underline{B_{\mathrm{r},k}}\mathrm{e}^{jk\theta} \\ B_{\theta}(\mathrm{R_{ag}},\theta) &= \sum_{k=-\infty}^{k=+\infty} \underline{B_{\theta,k}}\mathrm{e}^{jk\theta} \end{aligned} \tag{22}$$

Note that the time variation is included in the phase terms $\phi_{\theta,k}$ and $\phi_{\mathrm{r},k}$.

In the rest of the paper, the following notation is used:

$$\begin{aligned} F_k &= F_k(\mathrm{R_{ag}},\mathrm{R_s}) \\ E_k &= E_k(\mathrm{R_{ag}},\mathrm{R_s}) \end{aligned} \tag{23}$$

Then the magnetic flux density on the stator bore radius $\mathrm{R_s}$ can be expressed as:

$$\begin{aligned} B_{\mathrm{r}}(\mathrm{R_s},\theta) =& \frac{\mathrm{R_{ag}}}{\mathrm{R_s}} \sum_{k=-\infty}^{k=+\infty} \frac{F_k\underline{B_{\mathrm{r},k}} + jE_k\underline{B_{\theta,k}}}{2}\mathrm{e}^{jk\theta} \\ B_{\theta}(\mathrm{R_s},\theta) =& \frac{\mathrm{R_{ag}}}{\mathrm{R_s}} \sum_{k=-\infty}^{k=+\infty} \frac{F_k\underline{B_{\theta,k}} - jE_k\underline{B_{\mathrm{r},k}}}{2}\mathrm{e}^{jk\theta} \end{aligned} \tag{24}$$

The theoretic magnetic flux density on the stator bore radius $\mathrm{R_s}$ is obtained thanks to (24) which is based on the air-gap boundary condition (22). The expression (24) is different from what can be found in the literature because it is based on the magnetic flux density instead of magnetic potential [24,52]. Using the magnetic flux density is necessary in this paper since the AGSF expression (6) is based on the flux density.

Thus (24) gives the theoretical spatial transfer of the magnetic flux density $\mathbf{B}$ from the air-gap radius $\mathrm{R_{ag}}$ to the stator bore radius $\mathrm{R_s}$. The goal of the next sections is to deduce from (24) the theoretical spatial transfer law for the AGSF radial component.

3.2 Radial magnetic surface forces

The magnetic radial surface force density experienced by the outer structure (stator or rotor) is computed according to the AGSF formula 8 on a contour of radius $\mathrm{R_s}$ corresponding to the stator teeth tip radius as in Fig.2:

$$P_\mathrm{r}(\mathrm{R_s},\theta) = -\frac{B_\mathrm{r}(\mathrm{R_s},\theta)^2 - B_\theta(\mathrm{R_s},\theta)^2}{2\mu_0} \tag{25}$$

Note the sign of the equation taking into account the scalar product ($\mathbf{n}\cdot\mathbf{e}_\mathrm{r} = -1$) between the external normal to the surface Γ and the radial direction. The complex Fourier transform of P_r is performed using the convolution product:

$$\hat{P}_\mathrm{r}(\mathrm{R_s},n) = -\frac{\left[\hat{B}_\mathrm{r} \circledast \hat{B}_\mathrm{r}\right](\mathrm{R_s},n) - \left[\hat{B}_\theta \circledast \hat{B}_\theta\right](\mathrm{R_s},n)}{2\mu_0} \tag{26}$$

where $\hat{B}_\mathrm{r}$ and $\hat{B}_\theta$ are the complex Fourier transform of B_r and B_θ. Using properties of convolution product, $\hat{P}_\mathrm{r}$ is written as:

$$\hat{P}_\mathrm{r}(\mathrm{R_s},n) = -\left(\frac{\mathrm{R_{ag}}}{\mathrm{R_s}}\right)^2 \frac{1}{8\mu_0} \sum_{k=-\infty}^{k=+\infty} P_{\mathrm{r},k,n}\ \mathrm{e}^{jn\theta} \tag{27}$$

where $P_{\mathrm{r},k,n}$ is expressed using (24):

$$\begin{aligned} P_{\mathrm{r},k,n} = &\left(F_k F_{n-k} + E_k E_{n-k}\right) \underline{B_{\mathrm{r},k}}\ \underline{B_{\mathrm{r},n-k}} \\ &- \left(F_k F_{n-k} + E_k E_{n-k}\right) \underline{B_{\theta,k}}\ \underline{B_{\theta,n-k}} \\ &+ j\left(F_k E_{n-k} + E_k F_{n-k}\right) \underline{B_{\mathrm{r},k}}\ \underline{B_{\theta,n-k}} \\ &+ j\left(F_k E_{n-k} + E_k F_{n-k}\right) \underline{B_{\mathrm{r},n-k}}\ \underline{B_{\theta,k}} \end{aligned} \tag{28}$$

At this point, the spatial variation of each AGSF wavenumber is complex because it depends on the recombination of several magnetic flux density waves. Nevertheless, using polynomials properties of F_k and E_k, it can be shown:

$$\begin{cases} F_k F_{n-k} + E_k E_{n-k} = 2F_n \\ F_k E_{n-k} + E_k F_{n-k} = 2E_n \end{cases} \tag{29}$$

such that $P_{\mathrm{r},k,n}$ can be factorized:

$$\begin{aligned} P_{\mathrm{r},k,n} =& 2F_n \left(\underline{B_{\mathrm{r},k}}\ \underline{B_{\mathrm{r},n-k}} - \underline{B_{\theta,k}}\ \underline{B_{\theta,n-k}} \right) \\ &+ j2E_n \left(\underline{B_{\mathrm{r},k}}\ \underline{B_{\theta,n-k}} + \underline{B_{\mathrm{r},n-k}}\ \underline{B_{\theta,k}} \right) \end{aligned} \tag{30}$$

The convolution product is used to factorize the sum:

$$\begin{aligned} \sum_{k=-\infty}^{k=+\infty} P_{\mathrm{r},k,n} =& 2F_n \left[\hat{B}_{\mathrm{r}} \circledast \hat{B}_{\mathrm{r}} \right] (\mathrm{R_{ag}}, n) + 2F_n \left[\hat{B}_{\theta} \circledast \hat{B}_{\theta} \right] (\mathrm{R_{ag}}, n) \\ &+ j4E_n \left[\hat{B}_{\mathrm{r}} \circledast \hat{B}_{\theta} \right] (\mathrm{R_{ag}}, n) \end{aligned} \tag{31}$$

Replacing this intermediate result in (27) leads to:

$$\begin{aligned} \hat{P}_{\mathrm{r}}(\mathrm{R_s}, n) =& -\frac{1}{2} \left(\frac{\mathrm{R_{ag}}}{\mathrm{R_s}} \right)^2 F_n \frac{1}{2\mu_0} \left(\left[\hat{B}_{\mathrm{r}} \circledast \hat{B}_{\mathrm{r}} \right] (\mathrm{R_{ag}}, n) - \left[\hat{B}_{\theta} \circledast \hat{B}_{\theta} \right] (\mathrm{R_{ag}}, n) \right) \\ &- j\frac{1}{2} \left(\frac{\mathrm{R_{ag}}}{\mathrm{R_s}} \right)^2 E_n \frac{1}{\mu_0} \left[\hat{B}_{\mathrm{r}} \circledast \hat{B}_{\theta} \right] (\mathrm{R_{ag}}, n) \end{aligned} \tag{32}$$

Then the air-gap MST terms (8) are identified:

$$\hat{P}_{\mathrm{r}}(\mathrm{R_s}, n) = \left(\frac{\mathrm{R_{ag}}}{\mathrm{R_s}} \right)^2 \frac{F_n \hat{P}_{\mathrm{r}}(\mathrm{R_{ag}}, n) + jE_n \hat{P}_{\theta}(\mathrm{R_{ag}}, n)}{2} \tag{33}$$

Introducing the self-transfer coefficient S_n:

$$S_n = \left(\frac{\mathrm{R_{ag}}}{\mathrm{R_s}} \right)^2 \frac{F_n}{2} = \frac{1}{2} \left(\frac{\mathrm{R_{ag}}}{\mathrm{R_s}} \right)^{n+2} + \frac{1}{2} \left(\frac{\mathrm{R_{ag}}}{\mathrm{R_s}} \right)^{-n+2} \tag{34}$$

and the cross-transfer coefficient C_n:

$$C_n = \left(\frac{\mathrm{R_{ag}}}{\mathrm{R_s}} \right)^2 \frac{E_n}{2} = \frac{1}{2} \left(\frac{\mathrm{R_{ag}}}{\mathrm{R_s}} \right)^{n+2} - \frac{1}{2} \left(\frac{\mathrm{R_{ag}}}{\mathrm{R_s}} \right)^{-n+2} \tag{35}$$

the formula (33) can be rewritten under the form:

$$\hat{P}_{\mathrm{r}}(\mathrm{R_s}, n) = S_n \hat{P}_{\mathrm{r}}(\mathrm{R_{ag}}, n) + jC_n \hat{P}_{\theta}(\mathrm{R_{ag}}, n) \tag{36}$$

which demonstrates the radial part of (43). Note that the limit case $\mathrm{R_{ag}} = \mathrm{R_s}$ leads to $S_n = 1$ and $C_n = 0$ such that $\hat{P}_{\mathrm{r}}(\mathrm{R_s}, n) = \hat{P}_{\mathrm{r}}(\mathrm{R_{ag}} = \mathrm{R_s}, n)$. Thus, the formula stays valid.

3.3 Tangential magnetic surface forces

The magnetic tangential surface force experienced by the outer structure is computed according to the MST formula:

$$P_\theta(\mathrm{R_s},\theta) = -\frac{B_\mathrm{r}(\mathrm{R_s},\theta)B_\theta(\mathrm{R_s},\theta)}{\mu_0} \tag{37}$$

The methodology is very similar to the radial case. The complex Fourier transform of P_θ is performed using the convolution product:

$$\hat{P}_\mathrm{r}(\mathrm{R_s},n) = -\frac{\left[\hat{B}_\mathrm{r} \circledast \hat{B}_\theta\right](\mathrm{R_s},n)}{\mu_0} \tag{38}$$

which can be rewritten as:

$$\hat{P}_\theta(\mathrm{R_s},n) = -\frac{1}{4\mu_0}\left(\frac{\mathrm{R_{ag}}}{\mathrm{R_s}}\right)^2 \sum_{k=-\infty}^{k=\infty} P_{\theta,k,n}\ \mathrm{e}^{jn\theta} \tag{39}$$

with $P_{\theta,r,n}$ expressed using (24)

$$\begin{aligned} P_{\theta,k,n} =& 2F_n \underline{B_{\mathrm{r},k}}\ \underline{B_{\theta,n-k}} \\ &- jE_n\left(\underline{B_{\mathrm{r},k}}\ \underline{B_{\mathrm{r},n-k}} - \underline{B_{\theta,k}}\ \underline{B_{\theta,n-k}}\right) \end{aligned} \tag{40}$$

Replacing this intermediate result in (39) leads to:

$$\begin{aligned} \hat{P}_\theta(\mathrm{R_s},n) = -\left(\frac{\mathrm{R_{ag}}}{\mathrm{R_s}}\right)^2 \Bigg(& E_n \frac{1}{2\mu_0}\left[\hat{B}_\mathrm{r} \circledast \hat{B}_\theta\right](\mathrm{R_{ag}},n) \\ & + jF_n \frac{1}{4\mu_0}\Big(\left[\hat{B}_\mathrm{r} \circledast \hat{B}_\mathrm{r}\right](\mathrm{R_{ag}},n) \\ & - \left[\hat{B}_\theta \circledast \hat{B}_\theta\right](\mathrm{R_{ag}},n)\Big)\Bigg) \end{aligned} \tag{41}$$

Finally, identifying air-gap MST terms and using coefficients (34) and (35) leads to:

$$\hat{P}_\theta(\mathrm{R_s},n) = S_n\hat{P}_\theta(\mathrm{R_{ag}},n) - jC_n\hat{P}_\mathrm{r}(\mathrm{R_{ag}},n) \tag{42}$$

which demonstrates the tangential part of (43). Note that the limit case $\mathrm{R_{ag}} = \mathrm{R_s}$ leads to $S_n = 1$ and $C_n = 0$ such that $\hat{P}_\theta(\mathrm{R_s},n) = \hat{P}_\theta(\mathrm{R_{ag}} = \mathrm{R_s},n)$. Thus, the formula stays valid.

3.4 Discussion

This section aims to analyze the previous results in order to determine how it could affect the computed AGSF. In order to obtain the equations (42) and (36), an electrical machine with a cylindrical air-gap band was considered. A particular example with polar teeth was given in Fig. 2 but any machine topology could be considered. Equations (42) and (36) compose the new transfer law:

$$\begin{aligned} \hat{P}_{\mathrm{r}}(\mathrm{R_s}, n) &= S_n \hat{P}_{\mathrm{r}}(\mathrm{R_{ag}}, n) + jC_n \hat{P}_{\theta}(\mathrm{R_{ag}}, n) \\ \hat{P}_{\theta}(\mathrm{R_s}, n) &= S_n \hat{P}_{\theta}(\mathrm{R_{ag}}, n) - jC_n \hat{P}_{\mathrm{r}}(\mathrm{R_{ag}}, n) \end{aligned} \tag{43}$$

where S_n is called the self-transfer coefficient and C_n the cross-transfer coefficient:

$$\begin{aligned} S_n &= \frac{1}{2}\left\{ \left(\frac{\mathrm{R_{ag}}}{\mathrm{R_s}}\right)^{n+2} + \left(\frac{\mathrm{R_{ag}}}{\mathrm{R_s}}\right)^{-n+2} \right\} \\ C_n &= \frac{1}{2}\left\{ \left(\frac{\mathrm{R_{ag}}}{\mathrm{R_s}}\right)^{n+2} - \left(\frac{\mathrm{R_{ag}}}{\mathrm{R_s}}\right)^{-n+2} \right\} \end{aligned} \tag{44}$$

These coefficients S_n and C_n only depend on the considered magnetic surface force wavenumber n and the adimensional radius ratio $r = \frac{\mathrm{R_{ag}}}{\mathrm{R_s}}$. Thus the spatial variation of AGSF does not depend on a particular combination of magnetic flux density k^{th} wavenumbers but only on the considered AGSF wavenumber n. It also confirms that radial and tangential magnetic surface force are strongly correlated.

This result is a generalization of the simplified coefficients which were found in [35] but the new transfer coefficients include tangential surface force density and are valid for any kind of topology. The results of [35] can be found back assuming $P_{\theta}(\mathrm{R_s}, \theta) = 0 \ \forall \theta \in [0, 2\pi]$.

Fig. 6-7-8 illustrate the variation of the transfer coefficients (34) and (35) with the wavenumber n and the adimensional radius r. In particular, Fig. 6 highlights that:

$$\begin{aligned} \lim_{|n|\to\infty} |S_n| &= \infty \\ \lim_{|n|\to\infty} |C_n| &= \infty \end{aligned} \tag{45}$$

Theoretically the number of wavenumber in the air-gap is not infinite such

that:

$$\begin{aligned} \lim_{|n|\to\infty} |S_n \hat{P}_{\mathrm{r}}(\mathrm{R_{ag}}, n) + jC_n \hat{P}_{\theta}(\mathrm{R_{ag}}, n)| = 0 \\ \lim_{|n|\to\infty} |S_n \hat{P}_{\theta}(\mathrm{R_{ag}}, n) - jC_n \hat{P}_{\mathrm{r}}(\mathrm{R_{ag}}, n)| = 0 \end{aligned} \tag{46}$$

Nevertheless, the computation of numerical FFT does not provide an exact zero at every non-physical frequency. Then it is recommended to take precautions to avoid numerical noise amplification at high wavenumbers.

As illustrated in Fig. 6, the transfer coefficients have the following symmetry properties:

$$\begin{aligned} S_{-n} &= S_n \\ C_{-n} &= -C_n \end{aligned} \tag{47}$$

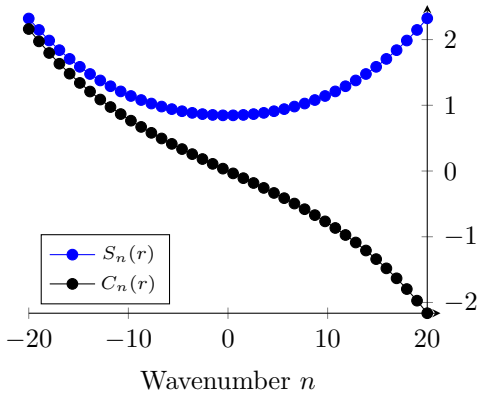

Figure 6: Transfer coefficients at a fixed relative radius $r = \frac{\mathrm{R_{ag}}}{\mathrm{R_s}} = 0.96$

The resultant electromagnetic torque is independent of the radius, as expected from the MST:

$$\begin{aligned} M_{\mathrm{z}}(\mathrm{R_s}) &= \int_0^{2\pi} P_{\theta}(\mathrm{R_s}, \theta)\mathrm{R_s^2}\ \mathrm{d}\theta \\ &= 2\pi \hat{P}_{\theta}(\mathrm{R_s}, 0)\mathrm{R_s^2} \\ &= 2\pi \left(\frac{\mathrm{R_{ag}}}{\mathrm{R_s}}\right)^2 \hat{P}_{\theta}(\mathrm{R_{ag}}, 0)\mathrm{R_s^2} \quad = M_z(\mathrm{R_{ag}}) \end{aligned} \tag{48}$$

The authors recall that this result is valid for any closed path in the airgap according to the Stoke's theorem. However, the total radial F_{r} or total

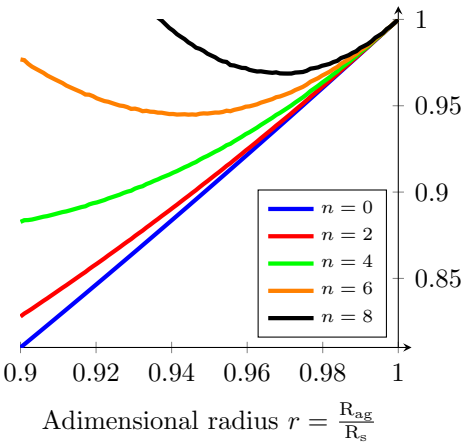

Figure 7: Self-transfer coefficient $S_n(r)$ as a function of adimensional radius r

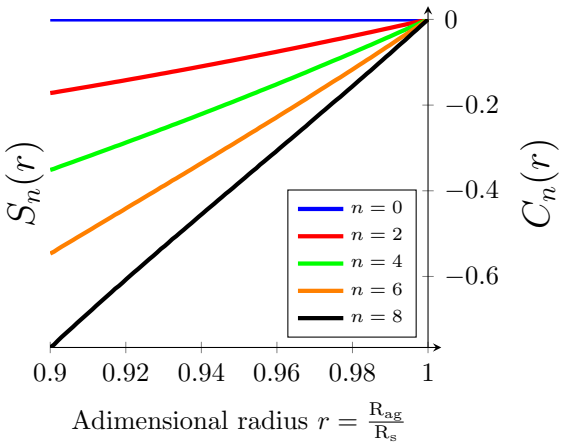

Figure 8: Cross-transfer coefficient $C_n(r)$ as a function of adimensional radius r

tangential F_t forces computed with AGSF depends on the radius :

$$\begin{aligned} F_{\mathrm{r}}(\mathrm{R_s}) &= \int_0^{2\pi} P_{\mathrm{r}}(\mathrm{R_s}, \theta)\ \mathrm{R_s}\ \mathrm{d}\theta \\ &= 2\pi \hat{P}_{\mathrm{r}}(\mathrm{R_s}, 0)\ \mathrm{R_s} \\ &= 2\pi \left(\frac{\mathrm{R_{ag}}}{\mathrm{R_s}}\right)^2 \hat{P}_{\mathrm{r}}(\mathrm{R_{ag}}, 0)\ \mathrm{R_s} \quad = \frac{\mathrm{R_{ag}}}{\mathrm{R_s}} F_{\mathrm{r}}(\mathrm{R_{ag}}) \end{aligned} \tag{49}$$

and similarly:

$$F_{\theta}(\mathrm{R_s}) = \frac{\mathrm{R_{ag}}}{\mathrm{R_s}} F_{\theta}(\mathrm{R_{ag}}) \tag{50}$$

Indeed, the Stoke's theorem is theoretically valid for global forces F_x and F_y in the fixed Cartesian coordinate frame:

$$\begin{aligned} F_{\mathrm{x}}(\mathrm{R_s}) &= \int_0^{2\pi} \left(P_{\mathrm{r}}(\mathrm{R_s}, \theta)\cos(\theta) - P_{\theta}(\mathrm{R_s}, \theta)\sin(\theta)\right)\ \mathrm{R_s}\ \mathrm{d}\theta = F_{\mathrm{x}}(\mathrm{R_{ag}}) \\ F_{\mathrm{y}}(\mathrm{R_s}) &= \int_0^{2\pi} \left(P_{\mathrm{r}}(\mathrm{R_s}, \theta)\sin(\theta) + P_{\theta}(\mathrm{R_s}, \theta)\cos(\theta)\right)\ \mathrm{R_s}\ \mathrm{d}\theta = F_{\mathrm{y}}(\mathrm{R_{ag}}) \end{aligned} \tag{51}$$

Nevertheless, in most of electrical machines $\frac{\mathrm{R_{ag}}}{\mathrm{R_s}} \approx 1$ such that the approximations $F_{\mathrm{r}}(\mathrm{R_s}) \approx F_{\mathrm{r}}(\mathrm{R_{ag}})$ and $F_{\theta}(\mathrm{R_s}) \approx F_{\theta}(\mathrm{R_{ag}})$ can be used accurately for

vibroacoustic assessment [14,33]. Indeed the air-gap cylindrical band thickness g is generally very small compared to the stator bore radius $\mathrm{R_s}$ such that the following approximations can be made:

$$\begin{aligned} S_n &\approx 1 \\ C_n &\approx -n\frac{\mathrm{g}}{\mathrm{R_s}} \end{aligned} \tag{52}$$

These approximations allow to have an a priori estimation of the transfer error on the computed AGSF. To illustrate the relevance of this estimation, an electrical machine with a single wavenumber excitation n is considered:

$$\begin{aligned} \hat{P}_{\mathrm{r}}(\mathrm{R_s}, n) &= jM\hat{P}_{\theta}(\mathrm{R_{ag}}, n) \\ \frac{\mathrm{g}}{\mathrm{R_s}} &= \frac{1}{Q} \end{aligned} \tag{53}$$

where $M \gg 1$ and $Q \gg 1$ are adimensional coefficients. Introducing (52) in (36) and (42) leads to:

$$\begin{aligned} |\hat{P}_{\mathrm{r}}(\mathrm{R_s}, n)| &\approx |\hat{P}_{\mathrm{r}}(\mathrm{R_{ag}}, n)| \\ |\hat{P}_{\theta}(\mathrm{R_s}, n)| &\approx \left(1 + n\frac{M}{Q}\right) |\hat{P}_{\theta}(\mathrm{R_{ag}}, n)| \end{aligned} \tag{54}$$

It means that depending on the $\frac{M}{Q}$ ratio, the transfer coefficients could have a great influence on the tangential magnetic force. A numerical application with the topology studied in [33] shows that $\frac{M}{Q} \approx \frac{1}{10}$ such that there could be a 40% error on the 4^{th} wavenumber.

In summary, the transfer law (43) was demonstrated. Then the transfer coefficients were analyzed. In particular Taylor expansions were performed to show that the transfer law effect on AGSF is not necessarily negligible. Consequently, a more detailed numerical study is carried out in the following section.

4 Application to electrical machines

In order to check if the transfer law (43) can have a non-negligible impact on the vibroacoustic behaviour of an electrical machine, this section presents two numerical applications:

- An induction machine with a constructive effect of coefficients (43).
- A synchronous machine with a destructive effect of coefficients (43).

As the aim of this section is to numerically validate the new transfer law, a reference is required. As discussed in [33], the nodal forces based on Virtual Work Principle (VWP) [9] is commonly assumed to be the most accurate method for magnetic force computation because it has shown to be robust with respect to formulation: according to [53] the VWP requires only one field component either $\mathbf{H}$ (in scalar potential ϕ-formulation) or $\mathbf{B}$ (in vector potential A-formulation) to compute magnetic forces.

However, the VWP output physical unit is in [N/m] for a 2D FEA simulation, while the AGSF gives [N/m^2]. The next section proposes a methodology to build equivalent surface fore density from VWP result.

4.1 Virtual Work Principle equivalent surface force

According to [54], the nodal force computed with the VWP concentrate the effects of the actual force density in the direct vicinity of the node. As a consequence, a nodal force is meaningful only on its original mesh. Then VWP nodal forces must be converted in order to be compared with the MST which is a surface force density defined on a contour in the air-gap.

The proposed method consists in summing all the nodal forces from VWP included in an angular opening $\mathrm{d}\theta$ to get the corresponding total force $F_{\mathrm{d}\theta}$ as shown in Fig 9. Then the obtained force is divided by the equivalent tooth tip surface:

$$P_{\mathrm{d}\theta} = \frac{F_{\mathrm{d}\theta}}{\mathrm{R_s d}\theta} \tag{55}$$

The computed magnetic surface force density depends on the radius of the targeted surface, but this is not a problem if the barycenter of the forces is very close to $\mathrm{R_s}$ [33]. The idea is to apply this process according to the discretization of the air-gap MST such that a surface force density $P_{\mathrm{vwp}}(\theta)$ $\forall\theta \in [0, 2\pi]$ is obtained on the stator bore radius $\mathrm{R_s}$.

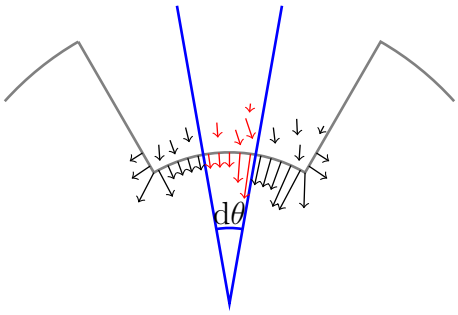

Figure 9: Summing all nodal forces (red arrows) on an angular opening dθ to get an equivalent surface force density at stator bore radius.

4.2 Validation with SCIM

In this section different methods for computing the magnetic radial and tangential surface force density are compared. The simulation was performed with FEA using MANATEE-FEMM coupling [41,55]. The authors remind that FEMM simulations are performed using a potential vector A-formulation.

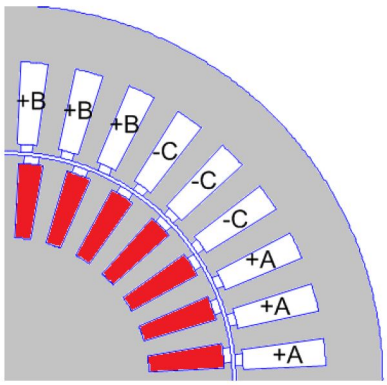

Figure 10: Analyzed cage rotor induction machine with single layer winding and stator/rotor semiclosed slots (one pole). [25]

A topology where the air-gap MST is commonly used to compute magnetic surface forces is the squirrel-cage induction machine (SCIM) characterized by a thin cylindrical air-gap band ($\frac{g}{R_s} \approx 1\%$). In particular, the studied SCIM topology is presented in Fig. 10.

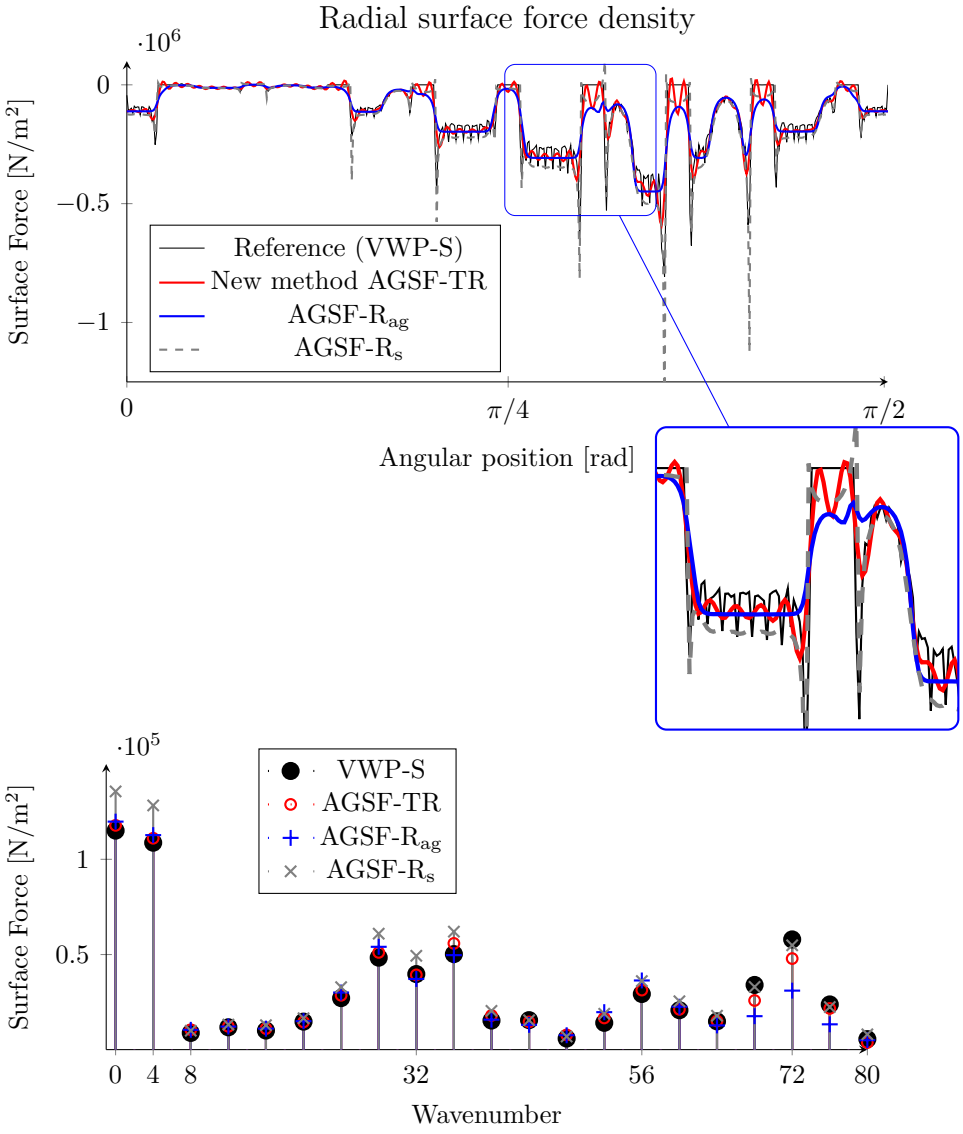

Figure 11: Comparison of several methods for radial surface force density using air-gap MST and VWP for SCIM topology.

The magnetic AGSF is computed according to different methods named as follow:

- VWP-S: the reference is the VWP equivalent surface force density as

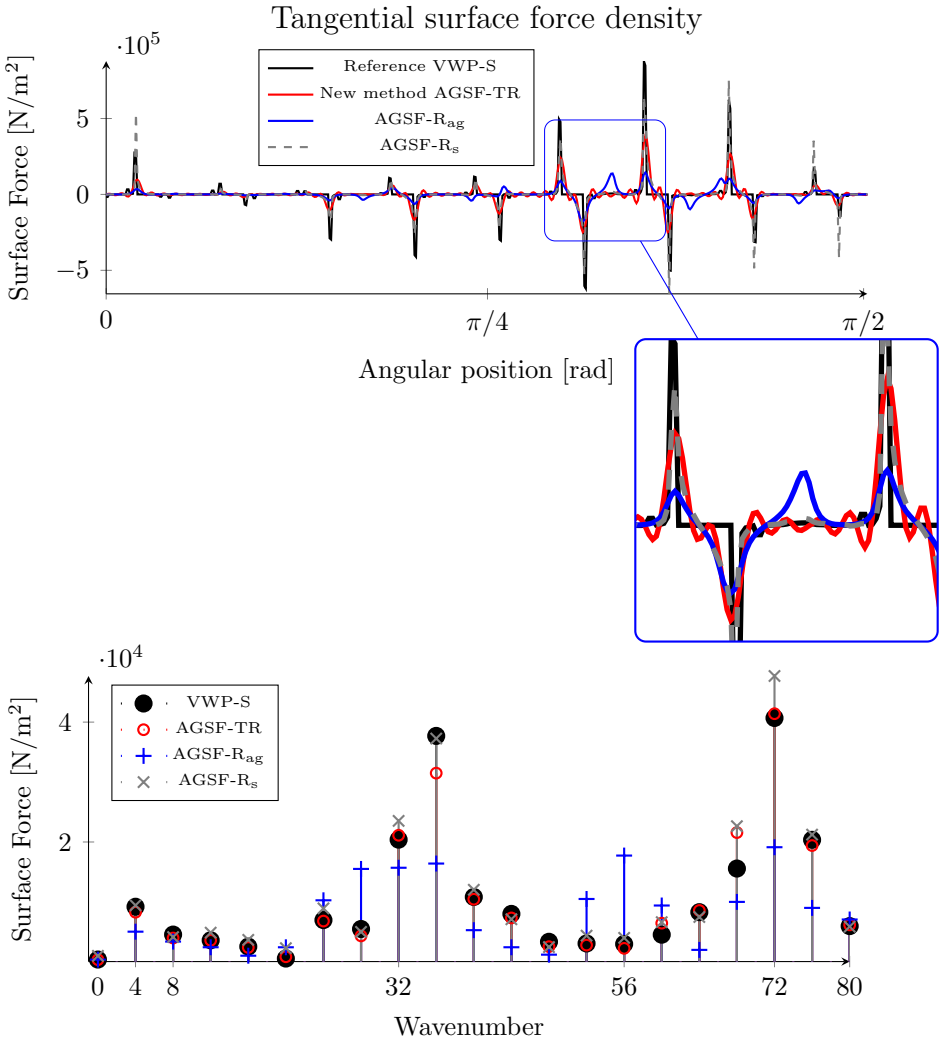

Figure 12: Comparison of several methods for tangential surface force density using air-gap MST and VWP for SCIM topology.

presented in Section 4.1;

- AGSF-TR: the new method to transfer AGSF (6) from R_{ag} to R_s using transfer coefficients (43);
- AGSF-R_{ag}: AGSF (6) applied on a circular contour at radius R_{ag} in

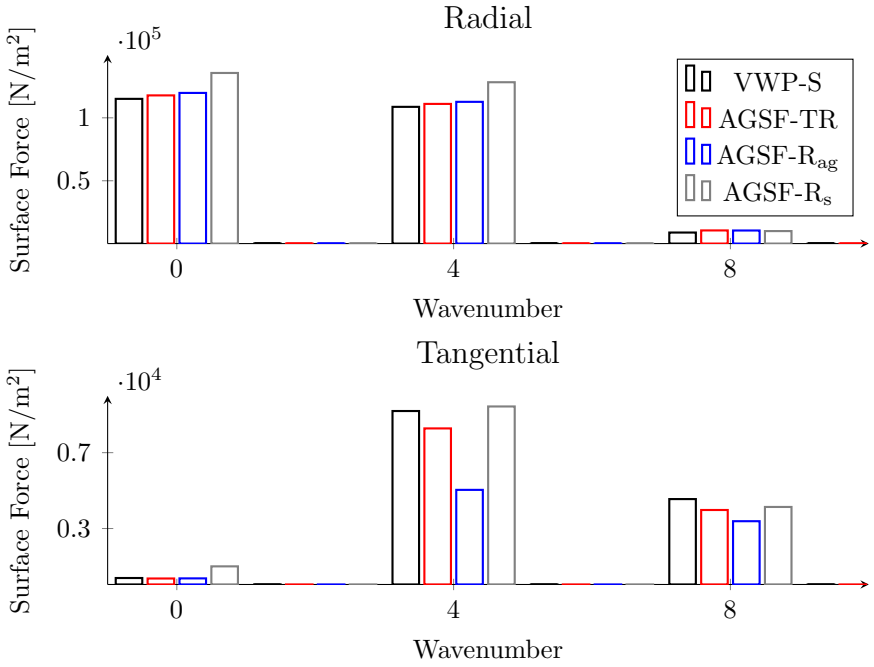

Figure 13: Comparison of several methods for surface force density for low wavenumbers with SCIM topology.

the middle of the air-gap cylindrical band;

- AGSF-R_s: AGSF (6) applied on a circular contour at a radius $r = 0.9997$ R_s i.e. cutting through the first layer of air-gap element at the tooth tip.

The results are presented in Fig. 11 for the radial direction and in Fig. 12 for the tangential direction. In particular Fig. 13 focuses on the force lower wavenumbers of interest for vibroacoustic analysis.

A global observation of the results indicates the AGSF-R_{ag} is giving more accurate radial surface force than AGSF-R_s for low wavenumbers. However the AGSF-R_s is more accurate than AGSF-R_{ag} for tangential surface force. In both directions, the AGSF-TR is accurate. In order to quantify these observations, a norm is defined to quantify the deviation from the VWP-S

method:

$$\|\hat{P} - \hat{P}_{\text{vwp}}\|_N = \sum_{k=-N}^{k=+N} |\hat{P}(k) - \hat{P}_{\text{vwp}}(k)| \tag{56}$$

The 8 first wavenumbers have the main contribution to the total vibration. Then, two applications of (56) can be defined:

- $\|.\|_8$ with the 8 first wavenumbers.
- $\|.\|_{254}$ with all available wavenumbers.

It leads to the numerical values of Table 1 for radial AGSF and Table 2 for tangential AGSF. In all case, the most accurate method is the AGSF-TR based on the new transfer law (43).

Table 1: Deviation of the magnetic surface force [N/m^2] with respect to the VWP-S in the radial direction

Method	$\|.\|_8$	$\|.\|_{254}$
AGSF-TR	1.3e+4	4.7e+5
AGSF-R_{ag}	1.8e+4	8.8e+5
AGSF-R_s	6.3e+4	6.3e+5

Table 2: Deviation of the magnetic air-gap surface force [N/m^2] with respect to the VWP-S in the tangential direction

Method	$\|.\|_8$	$\|.\|_{254}$
AGSF-TR	3.3e+3	4.1e+5
AGSF-R_{ag}	1.1e+4	8.9e+5
AGSF-R_s	4.0e+3	5.0e+5

The benefits of the transfer coefficients used with AGSF-TR is particularly well shown in Fig. 13 where the 4^{th} wavenumber of the tangential AGSF is initially wrongly estimated with the AGSF-R_{ag} method. When using the AGSF-TR method based on (43), the 4^{th} wavenumber of the radial surface force has a constructive interference with the 4^{th} wavenumber of the tangential surface force in the air-gap thanks to the cross-transfer coefficient.

As the air gap is thin, the previous results shows that the effect of transfer law (43) remains weak on the radial AGSF. However, the effect of the transfer law is not negligible on the tangential AGSF and leads to a clear improvement.

4.3 Application with SPMSM

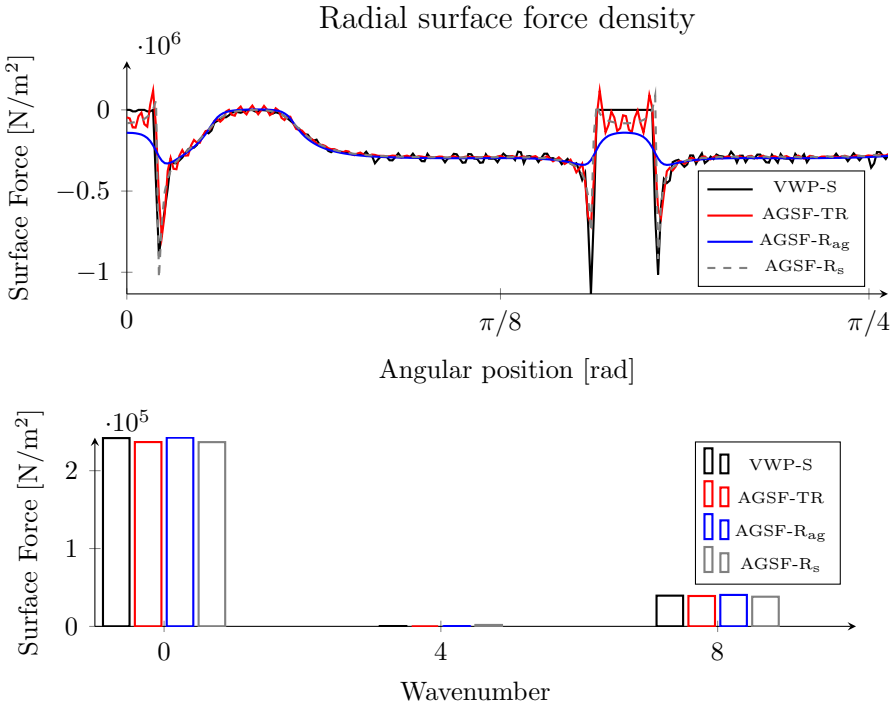

Figure 14: Comparison of several methods for radial surface force density using AGSF and VWP for SPMSM topology..

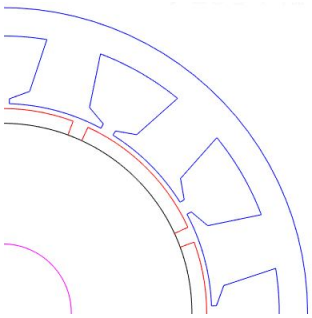

Figure 15: Analyzed surface permanent magnet synchronous machine with 12 slots and 8 poles

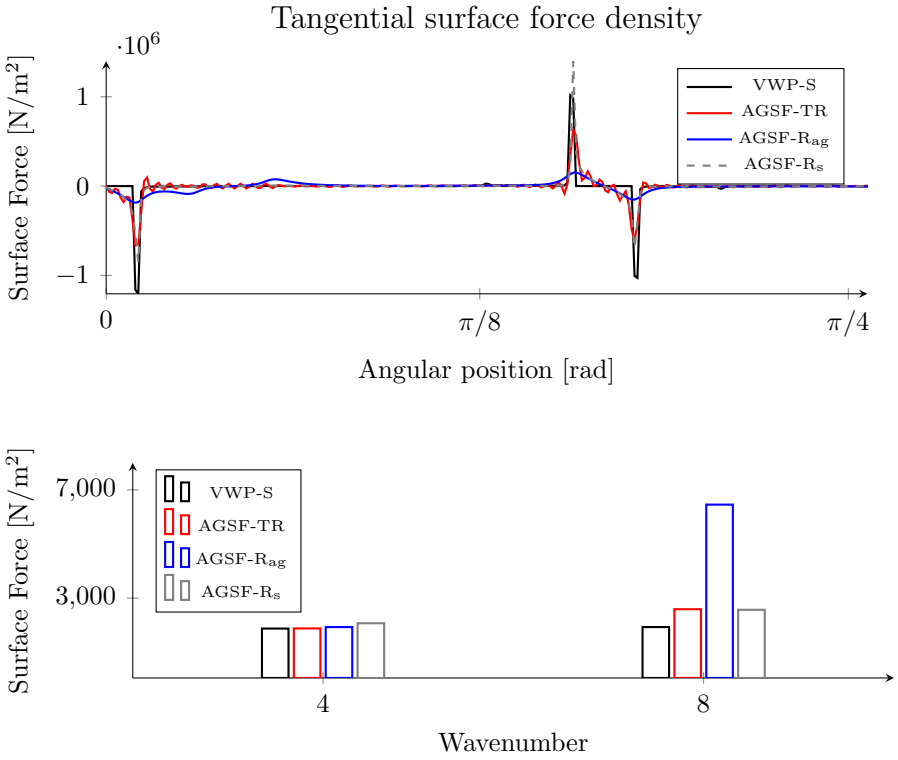

Figure 16: Comparison of several methods for tangential surface force density using AGSF and VWP for SPMSM topology.

This section proposes to compare the result of the different methods with a Surface Permanent Magnet Synchronous Machine (SPMSM) topology. The topology used for this application is similar to [32], except that the pole pairs number was fixed at 8 and the simulation was performed at no-load as shown in Fig. 15. In these conditions, Fig. 14 and Fig. 16 give an image of the magnetic AGSF. The impact of the cross-transfer coefficients is noticeable: the 8^{th} wavenumber of the radial AGSF in Fig. 14 has a destructive interference with the 8^{th} wavenumber of the tangential surface force in the air-gap. Thus the contribution of the cross-transfer coefficient (44) is again not negligible.

5 Conclusion

The purpose of this paper was to improve the accuracy of the air-gap surface forces computed with Maxwell Stress Tensor (MST) thanks to the analytical study of the air-gap magnetic field. The analytical solution of the electromagnetic field in the air-gap cylindrical band was used to demonstrate the existence of a new transfer law depending on the radius and the wavenumber. As expected, the transfer law has no impact on the torque calculation or the calculation of forces in the Cartesian coordinate frame. An induction machine as well as a synchronous machine were numerically simulated to evaluate the accuracy brought by the new transfer law on the magnetic air-gap surface force: it has a strong influence on the tangential surface force while remaining of little influence on the radial surface force for the studied topologies.

The transfer new law provides a rigorous way to calculate magnetic surface force on the teeth tip based on the middle air-gap surface force. As a consequence it allows to improve the accuracy of vibroacoustic prediction and troubleshoot with analytical magnetic models. Moreover, the transfer law is also interesting with finite element analysis: the compromise between accuracy and numerical noise for magnetic surface force - by choosing a radius of computation - is not an issue anymore.

The transfer law opens the possibility to compute surface force based on Maxwell Stress Tensor with large equivalent air-gap machines such as salient pole alternators or switched reluctance machines. Future research work will concern the compatibility of the method with mechanical models: a fast vibro-acoustic method should be developed in order to take into account the distribution of magnetic forces in the slots. The extension to outer rotor permanent magnet machines is also in the scope.

A Nomenclature

	Magnetic symbols
μ	Magnetic permeability [H/m]
μ_0	Magnetic permeability in free space [H/m]
$\mathbf{B}$	Magnetic flux density vector [T]
B_r, B_θ	Radial & tangential magnetic flux density components
$\mathbf{H}$	Magnetic field vector [A/m]
H_r, H_θ	Radial & tangential magnetic field components
$\mathbf{T}_\mathrm{m}$	Magnetic Stress Tensor [$\mathrm{A^2H/m^3}$]
$\mathbf{P}$	Magnetic surface force density [$\mathrm{N/m^2}$]
P_r, P_θ	Radial and tangential polar components of $\mathbf{P}$ [$\mathrm{N/m^2}$]
$\mathbf{F}_\mathrm{m}$	Magnetic force [N]
S_n	Self-transfer coefficient for air-gap surface force
C_n	Cross-transfer coefficient for air-gap surface force
	Mathematical symbols
$\hat{X}$	Complex Fourier transform of a field X
$\circledast$	Convolution product
$\mathbb{R}$	Space of real numbers
$\mathbb{N}$	Space of natural numbers
$\mathbb{C}$	Space of complex numbers
j	Imaginary number
u_s	Projection of a $\mathbf{u}$ vector onto the s direction
$\int_\Gamma$	Integral on a domain Γ
$\nabla.\mathbf{u}$	Divergence operator applied to a vector/tensor $\mathbf{u}$
	Abbreviations
MST	Maxwell Stress Tensor
VWP	Virtual Work Principle
FEA	Finite Element Analysis
SCIM	Squirrel-Cage Induction Machine
SPMSM	Surface Permanent Magnet Synchronous Machine
AGSF	Air-Gap Surface Force

References

[1] J. R. Melcher, *Continuum electromechanics*. Cambridge, MA: MIT Press, 1981.

[2] A. Abdel-Razek, J. Coulomb, M. Feliachi, and J. Sabonnadiere, "The calculation of electromagnetic torque in saturated electric machines within combined numerical and analytical solutions of the field equations," *IEEE Trans. Magn.*, vol. 17, no. 6, pp. 3250–3252, 1981.

[3] J. Mizia, K. Adamiak, A. Eastham, and G. Dawson, "Finite element force calculation: comparison of methods for electric machines," *IEEE Trans. Magn.*, vol. 24, no. 1, pp. 447–450, 1988.

[4] G. Jang, J. Yoon, N. Park, and S. Jang, "Torque and unbalanced magnetic force in a rotational unsymmetric brushless dc motors," *IEEE Trans. Magn.*, vol. 32, no. 5, pp. 5157–5159, 1996.

[5] K. J. Meessen, J. J. H. Paulides, and E. A. Lomonova, "Force calculations in 3-D cylindrical structures using fourier analysis and the maxwell stress tensor," *IEEE Trans. Magn.*, vol. 49, pp. 536–545, jan 2013.

[6] F. N. H. Robinson, *Macroscopic electromagnetism*, vol. 57. Pergamon, 1973.

[7] R. E. Rosensweig, *Ferrohydrodynamics*. Cambridge University Press, 1985.

[8] F. Henrotte and K. Hameyer, "Computation of electromagnetic force densities: Maxwell stress tensor vs. virtual work principle," *J. Comput. Appl. Math.*, vol. 168, no. 1-2, pp. 235–243, 2004.

[9] J.-l. Coulomb and G. Meunier, "Finite Element implementation of Virtual Work Principal for magnetic or electric force and torque computation," *IEEE Trans. Magn.*, vol. 20, pp. 1894–1896, sep 1984.

[10] F. Henrotte, M. Felden, M. van der Giet, and K. Hameyer, "Electromagnetic force computation with the eggshell method," in *Proc. 14th International IGTE Symposium*, 2010.

[11] S. Sathyan, A. Belahcen, J. Kataja, F. Henrotte, A. Benabou, and Y. Le Menach, "Computation of Magnetic Forces Using Degenerated Air-Gap Element," *IEEE Trans. Magn.*, vol. 53, pp. 1–4, jun 2017.

[12] J. F. Gieras, C. Wang, and J. C. Lai, *Noise of polyphase electric motors*. CRC press, 2005.

[13] Shenbo Yu and Renyuan Tang, "Electromagnetic and mechanical characterizations of noise and vibration in permanent magnet synchronous machines," *IEEE Trans. Magn.*, vol. 42, pp. 1335–1338, apr 2006.

[14] A. Saito, M. Kuroishi, and H. Nakai, "Vibration prediction method of electric machines by using experimental transfer function and magnetostatic finite element analysis," *Journal of Physics: Conference Series*, vol. 744, no. 1, p. 012088, 2016.

[15] M. Boesing, B. Callan-Bartkiw, P. Kotter, O. Zirn, J. Berkemer, and K. Wegener, "Noise-Vibration-Harshness simulation of ultralight vehicle traction drives based on a universal modelling approach," in *8th Int. Conf. PEMD*, no. 2, pp. 6 .–6 .(1), IET, 2016.

[16] G. Bauw, B. Cassoret, R. Romary, and O. Ninet, "Damper winding for noise and vibration reduction of induction machine under sinusoidal conditions," *IJAEM*, vol. 57, pp. 13–21, apr 2018.

[17] X. Chen, Z. Deng, J. Hu, and T. Deng, "An analytical model of unbalanced magnetic pull for pmsm used in electric vehicle: Numerical and experimental validation," *IJAEM*, vol. 54, no. 4, pp. 583–596, 2017.

[18] X. Xu, Q. Han, and F. Chu, "Review of electromagnetic vibration in electrical machines," *Energies*, vol. 11, no. 7, 2018.

[19] S. Verma and A. Balan, "Determination of radial-forces in relation to noise and vibration problems of squirrel-cage induction motors," *IEEE Trans. Energy Convers.*, vol. 9, no. 2, pp. 404–412, 1994.

[20] A. Kiyoumarsi and M. R. H. Zadeh, "A new analytical technique for analysis of the rotor eccentricity in rotating electrical machines," *IJAEM*, vol. 30, no. 1-2, pp. 83–93, 2009.

[21] J. L. Besnerais, V. Lanfranchi, M. Hecquet, and G. Friedrich, "Permeance computation for determination of induction motor acoustic noise," *Przeglad Elektrotechniczny*, vol. 86, no. 5, pp. 91–94, 2010.

[22] Q. Souron, J. Le Besnerais, and M. Hecquet, "Analysis of electromagnetically-induced vibrations of electrical machines based on spatiogram technique," *IJAEM*, vol. 51, no. s1, pp. S23–S32, 2016.

[23] M. Azeem, M. Humza, and B. Kim, "Analytical investigation of air-gap flux density distribution of a pm vernier motor," *IJAEM*, vol. 59, no. 3, pp. 943–949, 2019.

[24] T. Lubin, S. Mezani, and A. Rezzoug, "Exact analytical method for magnetic field computation in the air gap of cylindrical electrical machines considering slotting effects," *IEEE Trans. Magn.*, vol. 46, no. 4, pp. 1092–1099, 2010.

[25] K. Boughrara, N. Takorabet, R. Ibtiouen, O. Touhami, and F. Dubas, "Analytical Analysis of Cage Rotor Induction Motors in Healthy, Defective, and Broken Bars Conditions," *IEEE Trans. Magn.*, vol. 51, no. 2, p. 8200317, 2015.

[26] K. Ramakrishnan, M. Curti, D. Zarko, G. Mastinu, J. J. Paulides, and E. A. Lomonova, "Comparative analysis of various methods for modelling surface permanent magnet machines," *IET Electr. Power Appl.*, vol. 11, no. 4, pp. 540–547, 2017.

[27] B. Cassoret, R. Corton, D. Roger, and J.-F. Brudny, "Magnetic noise reduction of induction machines," *IEEE Trans. Power Electron.*, vol. 18, no. 2, pp. 570–579, 2003.

[28] J. Boisson, F. Louf, J. Ojeda, X. Mininger, and M. Gabsi, "Analytical approach for mechanical resonance frequencies of high-speed machines," *IEEE Transactions on Industrial Electronics*, vol. 61, no. 6, pp. 3081–3088, 2014.

[29] M. Boesing, T. Schoenen, K. A. Kasper, and R. W. De Doncker, "Vibration Synthesis for Electrical Machines Based on Force Response Superposition," *IEEE Trans. Magn.*, vol. 46, pp. 2986–2989, aug 2010.

[30] M. Boesing and R. W. De Doncker, "Exploring a vibration synthesis process for the acoustic characterization of electric drives," *IEEE Trans. Ind. Appl.*, vol. 48, no. 1, pp. 70–78, 2012.

[31] W. Liang, *The investigation of electromagnetic radial force and associated vibration in permanent magnet synchronous machines*. PhD thesis, Cranfield University, 2017.

[32] H. Fang, D. Li, R. Qu, and P. Yan, "Modulation effect of slotted structure on vibration response in electrical machines," *IEEE Trans. Ind. Electron.*, vol. 66, pp. 2998–3007, April 2019.

[33] R. Pile, E. Devillers, and J. Le Besnerais, "Comparison of Main Magnetic Force Computation Methods for Noise and Vibration Assessment in Electrical Machines," *IEEE Trans. Magn.*, vol. 54, pp. 1–13, jul 2018.

[34] J. Hallal, F. Druesne, and V. Lanfranchi, "Study of electromagnetic forces computation methods for machine vibration estimation," in *ISEF, Ohrid, Macedonia, Sept*, pp. 12–14, 2013.

[35] R. Pile, G. Parent, E. Devillers, T. Henneron, Y. Le Menach, J. Le Besnerais, and J.-P. Lecointe, "Application Limits of the Airgap Maxwell Tensor," in *CEFC 2018*, 2018.

[36] K. Meessen, J. Paulides, and E. Lomonova, "Force calculations in 3-d cylindrical structures using fourier analysis and the maxwell stress tensor," *IEEE Trans. Magn.*, vol. 49, no. 1, pp. 536–545, 2013.

[37] R. Bjørk, A. Smith, and C. R. H. Bahl, "Analysis of the magnetic field, force, and torque for two-dimensional halbach cylinders," *J. Magn. Magn. Mater.*, vol. 322, no. 1, pp. 133–141, 2010.

[38] G. Green, *An essay on the application of mathematical analysis to the theories of electricity and magnetism*. Wezäta-Melins Aktiebolag, 1828.

[39] M. Li and D. A. Lowther, "Local electromagnetic force computation in the presence of numerical field errors," *IEEE Trans. Magn.*, vol. 45, pp. 1344–1347, March 2009.

[40] A. Bossavit, "Virtual power principle and maxwell's tensor: which comes first?," *COMPEL*, vol. 30, no. 6, pp. 1804–1814, 2011.

[41] D. Meeker, "Femm 4.2," *User's Manual*, 2015.

[42] S. Garvey and G. D. Le Flem, "Tangential forces matter," in *9th IEMDC*, no. 468, pp. 174–178, 1999.

[43] J. Roivainen, *Unit-wave response-based modeling of electromechanical noise and vibration of electrical machines*. PhD thesis, Helsinki University of Technology, 2009.

[44] Q. Souron, J. Le Besnerais, and M. Hecquet, "Analysis of electromagnetically-induced vibrations of electrical machines based on spatiogram technique," *IJAEM*, vol. 51, pp. S23–S32, apr 2016.

[45] J. Le Besnerais, *Reduction of magnetic noise in PWM supplied induction machines: low-noise design rules and multi-objective optimisation*. PhD thesis, Ecole Centrale de Lille, France, 2008.

[46] Z. Q. Zhu, Z. P. Xia, L. J. Wu, and G. W. Jewell, "Analytical Modeling and Finite-Element Computation of Radial Vibration Force in Fractional-Slot Permanent-Magnet Brushless Machines," *IEEE Trans. Ind. Appl.*, vol. 46, pp. 1908–1918, sep 2010.

[47] H. Lan, J. Zou, Y. Xu, and M. Liu, "Effect of local tangential force on vibration performance in fractional-slot concentrated winding permanent magnet synchronous machines," *IEEE Trans. Energy Convers.*, pp. 1–1, 2018.

[48] T. Hamiti, T. Lubin, L. Baghli, and A. Rezzoug, "Modeling of a synchronous reluctance machine accounting for space harmonics in view of torque ripple minimization," *Mathematics and Computers in Simulation*, vol. 81, no. 2, pp. 354–366, 2010.

[49] T. Lubin, S. Mezani, and A. Rezzoug, "Simple analytical expressions for the force and torque of axial magnetic couplings," *IEEE Trans. Energy Convers.*, vol. 27, no. 2, pp. 536–546, 2012.

[50] G. Malé, T. Lubin, S. Mezani, and J. Lévêque, "Analytical calculation of the flux density distribution in a superconducting reluctance machine with hts bulks rotor," *Mathematics and Computers in Simulation*, vol. 90, pp. 230–243, 2013.

[51] L. D. Landau and E. Lifshitz, "The classical theory of fields. vol. 2," *Course of theoretical physics*, 1975.

[52] K.-S. Lee, M. DeBortoli, M. Lee, and S. Salon, "Coupling finite elements and analytical solution in the airgap of electric machines," *IEEE Trans. Magn.*, vol. 27, no. 5, pp. 3955–3957, 1991.

[53] Z. Ren, "Comparison of Different Force Calculation Methods in 3D Finite Element Modelling," *IEEE Trans. Magn.*, vol. 30, no. 5, pp. 3471–3474, 1994.

[54] G. Parent, P. Dular, J.-P. P. Ducreux, and F. Piriou, "Using a galerkin projection method for coupled problems," *IEEE Trans. Magn.*, vol. 44, pp. 830–833, jun 2008.

[55] J. Le Besnerais, "Fast prediction of variable-speed acoustic noise due to magnetic forces in electrical machines," in *ICEM 2016*, (Lausanne), pp. 2259–2265, IEEE, sep 2016.